Soil Biology and Biochemistry 142 (2020) 107727

Contents lists available at ScienceDirect

Soil Biology and Biochemistry

journal homepage: http://www.elsevier.com/locate/soilbio

Nitrite accumulation and nitrogen gas production increase with decreasing temperature in urea-amended soils: Experiments and modeling

Rodney T. Venterea [a,b,*], Jeffrey A. Coulter [c], Timothy J. Clough [d]

[a] USDA-ARS, Soil and Water Management Unit, 1991 Upper Buford Circle, St. Paul, MN, 55108, USA
[b] Dept. Soil, Water, and Climate University of Minnesota, St. Paul, MN, 55108, USA
[c] Dep. of Agronomy and Plant Genetics, Univ. of Minnesota, St. Paul, MN, 55108, USA
[d] Faculty of Agriculture and Life Sciences, Lincoln Univ., PO Box, 85084, Lincoln, 7647, Canterbury, New Zealand

ARTICLE INFO

Keywords:
Ammonia
Fertilizer
Nitrification
Nitrous oxide
Nitric oxide
Urine

ABSTRACT

Nitrite (NO_2^-) accumulation and associated production of nitric oxide (NO) and nitrous oxide (N_2O) gases in soils amended with nitrogen (N) fertilizers are well documented, but there remains a poor understanding of their regulation and variation among soil types. We examined responses to urea inputs in two soils at five temperatures from 5 to 30 °C and developed a process-driven model to describe the dynamics. A microcosm system was used to measure ammonia gas (NH_3), ammonium (NH_4^+), NO_2^-, nitrate (NO_3^-), NO, N_2O and pH over 12 weeks. Unexpectedly, NO_2^-, NO and N_2O production tended to increase as soil temperature declined in both soils. The maximum NO_2^- concentration, or compensation point (*CP*), differed by soil type but the time required to reach *CP* decreased exponentially with increasing temperature in both soils. A two-step nitrification model ('*2SN*') accounted for interactions of ammonia-oxidation (*AmO*), nitrite oxidation (*NiO*), urea hydrolysis, NH_4^+ sorption, N gas production and pH dynamics. Both steps of nitrification (*AmO* and *NiO*) were modeled using NH_3 inhibition kinetics. The model adequately simulated the observed dynamics and temperature responses and showed that increased uncoupling of *AmO* and *NiO* at colder temperatures resulted from their differential temperature responses. The dynamics observed here may be important following high-rate and banded N fertilizer applications and in ruminant urine patches. The results may help explain elevated N_2O emissions observed under cold temperatures. The *2SN* model can account for interactions among multiple processes and may be useful for studying the effects of management practices and climate factors, including climate change scenarios, on soil N cycling.

1. Introduction

Nitrite (NO_2^-) is often overlooked in soil nitrogen (N) studies due to its frequent presence at low concentrations relative to ammonium (NH_4^+) and/or nitrate (NO_3^-). However, it has been known for decades that NO_2^- can accumulate and persist for weeks following N fertilizer application (Chapman and Liebig, 1952; Chalk et al., 1975). This phenomenon is most commonly observed following application of urea, the predominant form of N fertilizer globally, and anhydrous ammonia, an important N source in the USA (FAO, 2019). Nitrite also accumulates following deposition of ruminant urine (Clough et al., 2003). The association of elevated NO_2^- with nitric oxide (NO) and nitrous oxide (N_2O) gas production is also well-documented (Venterea and Rolston, 2000c; Tenuta and Beauchamp, 2003; Maharjan and Venterea, 2013; Ma et al., 2015). Nitrite accumulation is favored by elevated pH and NH_4^+, which together promote ammonia (NH_3) volatilization (*AmV*) (Clough et al., 2003). Thus, the conditions that favor NO_2^- are also conducive to N losses in multiple forms. However, our understanding of the underlying processes, and our ability to manage them, are limited.

It is generally agreed that NO_2^- accumulation results from a divergence, or 'uncoupling', of the two steps of nitrification, i.e., when *AmO* proceeds faster than *NiO* (Burns et al., 1995; Taylor et al., 2019). A long-standing hypothesis regarding nitrification uncoupling is that elevation of the dissolved NH_3 concentration inhibits *NiO* (Aleem and

Abbreviations: *AmO*, ammonia-oxidation; *AmOR*, ammonia-oxidation rate; *AmS*, ammonium sorption; *AmV*, ammonia volatilization; *CCI*, cumulative coupling index; *ICI*, instantaneous coupling index; *NiO*, nitrite oxidation; *NiOR*, nitrite oxidation rate; *CP*, nitrite compensation point; *CPt*, time to reach nitrite compensation point; *2SN*, two-step nitrification model; *UH*, urea hydrolysis.

* Corresponding author. USDA-ARS, Soil and Water Management Unit, St. Paul, MN, 55108, USA.
E-mail address: rod.venterea@usda.gov (R.T. Venterea).

https://doi.org/10.1016/j.soilbio.2020.107727
Received 23 August 2019; Received in revised form 7 January 2020; Accepted 19 January 2020
Available online 22 January 2020
0038-0717/Published by Elsevier Ltd.

Alexander, 1958; Stojanovic and Alexander, 1958). The inhibition of nitrification by NH_3, and other potential inhibitory substances, has been extensively studied in wastewater treatment systems where regulation of nitrification is critical to process control and treatment efficiency (Anthonisen et al., 1976). Several kinetic models that account for inhibition of *AmO* and/or *NiO* in wastewater systems have been evaluated (Carrera et al., 2004; Park and Bae, 2009) but such models have not been applied to simulate soil N dynamics.

A process-based model of nitrification and its potential inhibition by NH_3 in fertilizer or urine-amended soil must account for several interactions. Soil pH initially increases due to urea hydrolysis and then decreases as *AmV* and *AmO* proceed. The changing pH may control nitrification by regulating *AmV* losses and thus *AmO* substrate supply, and/or by regulating liquid-phase NH_3, which can inhibit nitrification in soil (Breuillin-Sessoms et al., 2017). At the same time, changing rates of both *AmV* and *AmO* can feedback to affect pH (Sherlock and Goh, 1985). Sorption of NH_4^+ onto soil surfaces also controls liquid-phase NH_3 (Venterea et al., 2015), and thus both *AmV* and nitrification. As NO_2^- accumulates, it can drive NO and N_2O production. Accounting for these interactions in a model is essential for testing hypotheses regarding soil N cycling dynamics following fertilizer application and ruminant urine deposition.

Temperature is a key variable driving most if not all processes regulating NO_2^- dynamics and associated N losses. While rates of these processes are generally expected to increase as temperature increases over the range of 0–30 °C, individual processes are likely to differ in their relative temperature responses (Moyo et al., 1989; Taylor et al., 2017; Lu et al., 2018). Thus, it is difficult to predict the net overall temperature effect on variables of interest, such as time-integrated or cumulative production of NO_2^-, NH_3, NO or N_2O. A model that can account for individual process responses and their interactions may aid in understanding how these net outcomes are affected by temperature over daily, seasonal or longer time scales. The objectives of this study were to quantify temperature effects on soil N cycling following high urea inputs in two soils under aerobic conditions, and to develop a process-based model to enable better prediction and understanding of NO_2^- accumulation and gaseous N losses.

2. Material and methods

2.1. Microcosm experiments

The soils used here (soils 'A' and 'B') were previously studied by Breuillin-Sessoms et al. (2017) and were selected for further study based on their contrasting properties. Soils were collected from research plots at the University of Minnesota research stations in fall 2017 from the upper 0.15 m in treatments that had received no N fertilizer during the previous growing season. Soil A was a Wheatville loam (Aeric Calciaquolls) with sand, silt and clay fractions of 43, 38 and 19%, pH (1:1 H_2O) of 8.2 and organic matter (loss on ignition) of 3.6%, collected from plots maintained in a soybean(*Glycine max* L.)-wheat (*Triticum aestivum*) rotation in Crookston, MN (47.80°N 96.61°W). Soil B was a Waukegan silt loam (Typic Hapludolls) with sand, silt and clay fractions of 26, 58 and 16%, pH (1:1 H_2O) of 6.8 and organic matter of 5.0%, collected from plots maintained in a corn (*Zea mays* L.)-soybean rotation in Rosemount, MN (44.75°N 93.07°W). Soils were dried at room temperature for 7–10 d, ground, sieved (2 mm), homogenized, and stored at 4 °C prior to use. The soil microcosm design used in previous studies to measure NH_4^+, NO_2^-, NO_3^-, N_2O and pH dynamics (Venterea et al., 2015; Breuillin--Sessoms et al., 2017) was extended to also measure NO production and NH_3 volatilization. A series of individual replicate soil microcosms were prepared, each consisting of 250-ml glass jars (70 mm diameter x 65 mm high) containing 10.0 g of air-dried soil spread in a 3 to 4-mm layer on the bottom of the jar. After weighing soil into each jar, a urea solution was mixed into each microcosm to deliver 500 μg N g^{-1} dry soil, to mimic initial conditions typically found following banded or high-rate N fertilizer application, or urine deposition (Maharjan and Venterea, 2013; Wells et al., 2015). As in the previous experiments, the volume of solution added was equivalent to ~50% water-filled pore space (0.25 and 0.29 g H_2O g^{-1} in soils A and B, respectively) in order to maintain primarily aerobic conditions. The wetted soil was distributed in an annular pattern at the bottom of each jar to allow placement of a glass beaker containing 15-ml of 0.05 M H_2SO_4 which served to capture gas-phase NH_3 that volatilized from the soil and convert it to NH_4^+, which was subsequently quantified as described below (Sánchez-Rodríguez et al., 2019).

Microcosms were sealed with metal lids and placed in dark incubators at temperatures of 5, 10, 15, 22 and 30 °C. Three replicate microcosms of each treatment were sacrificed for analysis periodically over 12 wk, starting on the day following addition of solutions. For experiments conducted at ≥15 °C, sampling was performed at 3 or 4-d intervals during the first 3 wk, and then weekly, except for the final (84-d) sampling. Due to lower rates of N transformation at 5 and 10 °C, sampling frequency was decreased accordingly. All microcosms were opened for 3 min within the first three days after adding solutions to release CO_2 produced by urea hydrolysis, and thereafter at 1 to 2-wk intervals. This procedure maintained O_2 levels in the microcosm headspace above 18%, as verified by periodic analysis using gas chromatography with a thermal conductivity detector.

Each sampling day, individual microcosms were analyzed in the following sequence: (1) volatilized NH_3: the acid solution was removed for analysis of NH_4^+ using a flow-through analyzer (Lachat, Loveland, CO) and the sodium salicylate-nitroprusside method (Mulvaney, 1996); (2) NO production: the jar was placed in an insulating-foam holder and sealed with a lid equipped with inlet and outlet fittings that directed flow of a NO-free airstream through the jar and into a chemiluminescent NO analyzer (NOA 280i, Zysense) (Venterea and Rolston, 2000a). Outlet NO concentration was monitored until steady (<5 min) and the production rate determined from the flow rate (0.20 l min^{-1}) and steady-state concentration; (3) N_2O production: the jar was placed unsealed into a water bath at the selected temperature for 5 min to allow the headspace to equilibrate with room air, and then sealed and placed back into the incubator for 60 min at which time the headspace was sampled by syringe through a septum. Gas samples were transferred to vials that were analyzed for N_2O concentration by gas chromatography (Agilent 5890) with electron capture detection. The N_2O production rate was determined from the change in headspace N_2O concentration; (4) Extractable NH_4^+: a subsample (~3 g) of soil was extracted with 20 ml of 2 M KCl for 1 h. Filtered extracts were analyzed for NH_4^+ per above; (5) pH: a subsample (~2 g) was mixed with an equal mass of 1M KCl for soil pH determination; (6) Extractable NO_2^- and NO_3^-: the remaining soil was extracted with alkaline 2 M KCl for 10 min (Stevens and Laughlin, 1995). Separate filtered extracts were analyzed for $NO_2^- + NO_3^-$ and NO_2^- within 2 h by flow-through analysis with the Greiss-Ilosvay method with and without Cd reduction, respectively (Mulvaney, 1996) and NO_3^- concentration was determined by difference accounting for Cd reduction efficiency.

Cumulative volatilization of NH_3 was determined from the mass of NH_4^+ captured in the acid-trapping solution at each sampling date. Cumulative production of NO and N_2O were calculated by trapezoidal integration of measured NO and N_2O production rates versus time, expressed in units of μg N g^{-1}. Cumulative NO_2^- was calculated by trapezoidal integration of measured NO_2^- concentrations versus time, expressed in units of μg N g^{-1} d (Maharjan and Venterea, 2013). Recoveries of N species at the end of the experiment were calculated as a percentage of the total N input, including 500 μg N g^{-1} of added urea plus simulated contributions from N mineralization (described below), which represented 1.5–5% of the total input. Cumulative variables were analyzed at $P \leq 0.05$ using the MIXED procedure of SAS (version 9.4, Cary, NC), with soil and temperature considered as fixed effects and replication and interactions with replication considered as random effects. Data for all variables were assessed for homogeneity of variance

and normality using scatterplots of residuals vs. predicted values (Kutner et al., 2004) and the UNIVARIATE procedure of SAS. Mean comparisons were made with pairwise *t* tests using the PDIFF option of the MIXED procedure.

2.2. Modeling

The *2SN* model is an expansion of a previous biochemical model (Venterea and Rolston, 2000b). Here, the model describes N and pH dynamics in a well-mixed, unsaturated and predominately aerobic soil volume where autotrophic nitrification predominates over heterotrophic denitrification. The model simulates several interacting components that are illustrated schematically in Fig. 1: (i) urea hydrolysis (*UH*), (ii) ammonium sorption (*AmS*) and equilibria, (iii) nitrification (*AmO* and *NiO*), (iv) NH_3 toxicity, (v) volatilization of NH_3 and production of NO and N_2O gases, (vi) pH dynamics and (vii) soil N mineralization (*NM*). The equations used to describe each process are presented below and the corresponding parameters used in the final version of the model are listed in Table 1.

The model is structured as a system of seven coupled differential equations that can be represented by:

$$\frac{dC_i}{dt} = P_i - [S_i] \tag{1}$$

where C_i is the concentration of the *i*th species, *t* is time, P_i and S_i are rates of production (source term) and consumption (sink term), respectively, and where $i = 1$ to 7 corresponds respectively to urea (*U*), total extractable ammoniacal N (NH_x), NO_2^- and NO_3^-, gaseous NO and N_2O, and hydrogen ion (H^+). The model allows the source and sink terms to be functions of any of the simulated species reflecting the coupled nature of the processes. An adaptive Runge-Kutta scheme (Press et al., 2010) was formulated in FORTRAN (Approximatrix) to simultaneously solve the system of equations.

At each time-step, the NH_x pool was partitioned into three simulated sub-pools, liquid-phase ammonium (NH_4^+L), sorbed-phase ammonium (NH_4^+S) and liquid-phase ammonia (NH_3L) using the method of Venterea et al. (2015) where the $NH_4^+L \leftrightarrow NH_3L$ equilibrium was regulated by pH and the pK_a for NH_4^+, and the $NH_4^+S \leftrightarrow NH_4^+L$ equilibrium was regulated by:

$$NH_4^+S = \frac{\mu_{AmS}\, NH_4^+L}{K_{AmS} + NH_4^+L} \tag{2}$$

where μ_{AmS} is the maximum sorption capacity and K_{AmS} is the half-saturation constant. Variation of pK_a with temperature was calculated based on Bates and Pinching (1949). At each time-step, total extractable NO_2^- was partitioned into unprotonated (NO_2^-) and protonated (HNO_2) sub-pools using the pKa for HNO_2 (Venterea and Rolston, 2000a). The model was compared to observed data for six of the seven main pools, NH_x, NO_2^-, NO_3^-, NO, N_2O, and H^+ (as pH) (excluding urea which was not measured) as well as cumulative volatilized NH_3. All processes except *AmS*, *NM*, *AmO* and *NiO* were simulated using first-order kinetics, where the rate coefficients are represented as *k* or α with a subscript identifying the process. Added *U* defines the initial condition, after which *U* dynamics are driven by *UH*:

$$\frac{dU}{dt} = -[k_{UH}U] \tag{3}$$

which serves as the main source for NH_x simulated by:

$$\frac{dNH_x}{dt} = k_{UH}U + NMR - [AmOR + k_{AmV}NH_3L] \tag{4}$$

where *NMR*, *AmOR* (Eq. (11)) and $k_{AmV}NH_3L$ are the rates of *NM*, *AmO* and *AmV*, respectively. Analysis of previously reported data (Breuillin-Sessoms et al., 2017) for these and six other soils incubated with no urea addition showed that *NMR* could be simulated by:

$$NMR = NMR_o \ \exp(-d * t) \tag{5}$$

where NMR_o is the rate at time $(t) = 0$ and *d* is a decay coefficient (details in Supplementary Information [SI]). Temperature variation of NMR_o was simulated with $Q_{10} = 1.61$ based on a global meta-analysis (Liu et al., 2017b). Nitrite was simulated using:

$$\frac{dNO_2^-}{dt} = AmOR - \left[NiOR + k_{NO}NO_2^* + k_{N_2O}NO_2^* + k_fNO_2\right] \tag{6}$$

where *NiOR* is the nitrite-oxidation rate (Eq. (12)), $k_{NO}NO_2^*$ is the NO production rate (Eq. (8)) and $k_{N_2O}NO_2^*$ is the NO_2^- -driven component of the N_2O production rate (Eq. (9)). The final term, k_fNO_2, accounts for NO_2^- fixation into soil organic matter (Thorn and Mikita, 2000; Fitzhugh et al., 2003) and/or NO_2^- -driven production of gases other than NO or N_2O (Stevenson and Swaby, 1964; Su et al., 2011). Nitrate NO_3^- was simulated by:

$$\frac{dNO_3^-}{dt} = NiOR \tag{7}$$

Production of NO and N_2O were simulated, respectively, by

$$\frac{dNO}{dt} = k_{NO}NO_2^* \tag{8}$$

$$\frac{dN_2O}{dt} = k_{N_2O}NO_2^* + b_{N_2O} \tag{9}$$

The NO_2^* designation indicates that both NO_2^- and HNO_2 were evaluated in separate simulations as the reactive substrate since production of NO and N_2O have been related to each of these substrates (Thorn and Mikita, 2000; Venterea and Rolston, 2000c, a; Venterea et al., 2005; Venterea, 2007). In Eq. (9), b_{N_2O} is a zero-order N_2O source observed

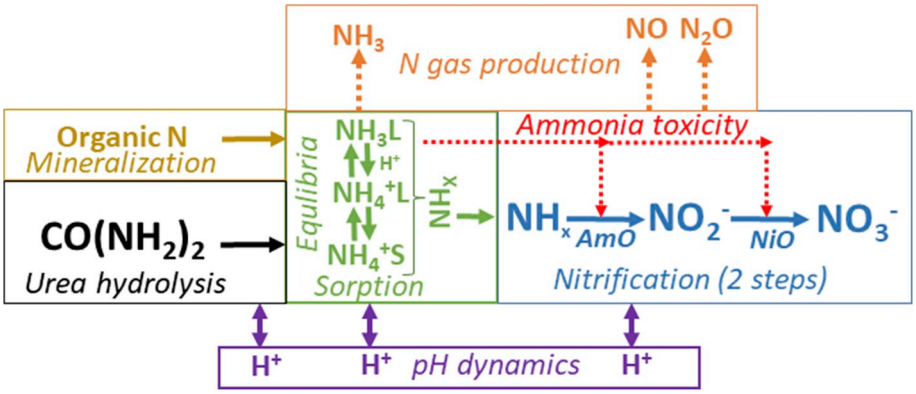

Fig. 1. Major components of the two-step nitrification (*2SN*) model.

Table 1
Parameters in the *2SN* model and their temperature dependencies.

Parameter		Units	Eq[a]	Soil A		Soil B	
				Value or function[b]	E_a[c]	Value or function[b]	E_a[c]
μ_{AmS}	Max. *AmS* capacity	μg N g^{-1}	2	1344[d]	n/a	1743[d]	n/a
K_{AmS}	*AmS* half-saturation	μg N ml^{-1}	2	152[d]	n/a	412[d]	n/a
k_{UH}	*UH* decay	h^{-1}	3	$0.022*1.75^{[(T-22)/10]}$	39.2 (0.6)	$0.024*1.50^{[(T-22)/10]}$	28.4 (0.4)
k_{AmV}	*AmV* coefficient	ml g^{-1} h^{-1}	4	0.19 ($T \leq 22$ °C) $0.026*T$ - 0.38 ($T > 22$ °C)	NS	$0.0695*T + 0.047$ ($T \leq 10$ °C) 0.74 ($T > 10$ °C)	NS
NMR_o	Initial *NM* rate	μg N g^{-1} h^{-1}	5	$0.022*1.61^{[(T-22)/10]}$ [e]	33.4 (0.5) [e]	$0.055*1.61^{[(T-22)/10]}$ [e]	33.4 (0.5) [e]
d	*NM* decay	h^{-1}	5	0.029[e]	n/a[e]	0.074[e]	n/a[e]
k_f	Inferred NO_2^- sink	h^{-1}	6	$2.25e^{-4}$ ($T \leq 10$ °C); $1.0e^{-3}$ ($T \geq 22$ °C) $6.5e^{-5}*T - 4.0e^{-4}$ (10 °C $< T <$ 22 °C)	49.8 (10.6)	$0.0005 + 0.0005*[1+exp^{(12.8-T)/1.33}]^{-1}$	21.1 (5.8)
k_{NO_g}	NO production	h^{-1}	8	0.074 ($T \leq 10$ °C) $0.58*[1-exp^{(-0.09*T)}]$ - 0.27 ($T > 10$ °C)	40.4 (9.1)	$0.250*T$-0.01 ($T \leq 10$ °C) $0.858*exp^{(0.020*T)}$ - 0.885 ($T > 10$ °C)	39.0 (8.7)
k_{N_2O}	N_2O production	h^{-1}	9	$-0.0025*T$ +0.04 ($T < 10$ °C) 0.0022*T-0.0069 ($T \geq 10$ °C)	46.6 (5.5) 10–30 °C	0.0127 ($T \leq 15$ °C) $0.0026*exp^{(0.108*T)}$ - 0.0007 ($T > 15$ °C)	48.7 (11.5)
b_{N_2O}	Background N_2O	ng g^{-1} h^{-1}	9	$0.0003*[1-exp^{(-0.205*T)}] + 0.98$	1.0 (0.001) 5–22 °C	$1.10*(1 + exp^{[(16.7\ -\ T)/0.973]})^{-1} + 1.23$	27.9 (5.9)
α_{UH}	pH rise, *UH*	$\frac{nM\ H^+}{\mu g\ N\ g^{-1}}$	10	0.14 ($T < 15$ °C); 0.15 ($T > 22$ °C) $0.0014*T$+ 0.12 (15 °C $\leq T \leq$ 22 °C)	NS	$0.475*exp^{(0.126*T)} + 3.14$ ($T \leq 15$ °C) 6.3 (15 °C $< T <$ 22 °C) $0.21*T + 1.60$ ($T \geq 22$ °C)	18.2 (3.0)
α_{AmV}	pH decline, *AmV*		10	1.0	n/a	$2.6 + 106*[1+exp^{(12.3-T)/2.81}]^{-1}$ (T ≤ 22 °C) 105 (T > 22 °C)	93.9 (22) 5–22 °C
α_{AmO}	pH decline, *AmO*		10	0.03	n/a	8.5	n/a
μ_{AmO}	Maximum *AmO* rate	μg N g^{-1} h^{-1}	11	0.135*T - 0.056 ($T < 15$ °C) $171*[1-exp^{(-0.28*T)}]$-166 ($T \geq 15$ °C)	57.6 (10.3)	$0.135*exp^{(0.094*T)}$+0.024	62.8 (1.8)
K_{AmO}	*AmO* half-saturation	μg N g^{-1}	11	106	n/a	25.0	n/a
KI_{AmO}	NH_3 inhibition of *AmO*	μg N ml^{-1}	11	420	n/a	103	n/a
μ_{NiO}	Maximum *NiO* rate	μg N g^{-1} h^{-1}	12	$0.059*exp^{(0.15\ T)}$ - 0.13 ($T < 22$ °C) 1.38 ($T \geq 22$ °C)	122 (26.1)	$0.168*exp^{(0.106*T)}$-0.244	108 (5.9)
K_{NiO}	*NiO* half-saturation	μg N g^{-1}	12	6.1	n/a	8.8	n/a
KI_{NiO}	NH_3 inhibition of *NiO*	μg N ml^{-1}	12	210	n/a	13.0	n/a
ε	$\mu_{AmO}^{t=0} : \mu_{AmO}^{max}$ ratio	–	13	0.20[f]	n/a	0.20[f]	n/a
β	*AmO* growth rate	d^{-1}	13	0.0034[f]	n/a	0.0013[f]	n/a

[a] Equation where parameter is first used.
[b] For parameters varying with temperature (T), equations for regression functions shown in Fig. 4 are given below. If a T range is not specified, functions apply over 5–30 °C.
[c] E_a = Activation energy (kJ mol^{-1}) (±std err). Unless specified, E_a applies over 5–30 °C. 'NS' = Arrhenius relationship is not significant at $P < 0.05$; 'n/a' = parameter constant with T.
[d] Parameter values reported by Breuillin-Sessoms et al. (2017).
[e] Values based on analysis of data from Breuillin-Sessoms et al. (2017) (see Supplemental Information). E_a for NMR_o calculated using $Q_{10} = 1.61$ from Liu et al. (2017).
[f] Eq. (13) was only used for simulations at 5 °C so no temperature dependencies were determined for ε and β.

when these soils were incubated aerobically with no urea added and where extractable NO_2^- remained at baseline levels (<0.1 μg N g^{-1}) (Breuillin-Sessoms et al., 2017). Soil pH was simulated in a largely empirical manner assuming production and consumption of H^+ were each first-order with respect to *UH*, *AmO* and *AmV*

$$\frac{dH^+}{dt} = \alpha_{AmOR} AmOR - [\alpha_{UH} k_{UH} U + \alpha_{AmV}\ k_{AmV} NH_3 L] \quad (10)$$

where the coefficients α_{AmOR}, α_{UH} and α_{AmV} account for production of H^+ from *AmO*, neutralization of H^+ during *UH* and shifting of the chemical equilibrium from *AmV*, respectively (Sherlock and Goh, 1985).

Preliminary analysis and simulations were done to examine different kinetic models for *AmOR* and *NiOR* including standard Michaelis-Menten kinetics and different formulations that account for inhibition by NH_3L (Park and Bae, 2009). Among these, the uncompetitive inhibition model selected by Park and Bae (2009) was found to best describe the NO_2^- dynamics:

$$AmOR = \frac{[NH_x]\mu_{AmO}}{[NH_x]\left(1 + \frac{[NH_3 L]}{KI_{AmO}}\right) + K_{AmO}} \quad (11)$$

$$NiOR = \frac{[NO_2^-]\mu_{NiO}}{[NO_2^-]\left(1 + \frac{[NH_3 L]}{KI_{NiO}}\right) + K_{NiO}} \quad (12)$$

where μ_{AmO} and μ_{NiO} are maximum oxidation rates, K_{AmO} and K_{NiO} are half-saturation constants and KI_{AmO} and KI_{NiO} are inhibition constants for *AmO* and *NiO*, respectively. Simulations were also performed using Eq. (11) amended with a term to allow μ_{AmO} to increase over time from an initial value (μ_{AmO}^0) to a maximum value (μ_{AmO}^{max}) according to:

$$\mu_{AmO}(t) = \varepsilon * \exp(\beta * t)\mu_{AmO}^{max} \quad (13)$$

where β is a growth rate coefficient and ε is the ratio between μ_{AmO}^0 and μ_{AmO}^{max} which reaches a value of 1.0 at $t = -\frac{\ln \varepsilon}{\beta}$.

The term 'compensation point' or 'compensation concentration' is used in a variety of contexts to indicate the point at which rates of opposing processes are in balance (Farquhar et al., 1980; Conrad, 1994). With respect to NO_2^-, the opposing processes are production via *AmO* and consumption via *NiO*, NO and N_2O production (and possibly other processes) where the overall gross consumption rate increases as NO_2^- concentration increases. Thus, the parameterized model was used to calculate the NO_2^- compensation point (*CP*) and the corresponding time (*CPt*) at which the *CP* was reached, where *CP* is the NO_2^- concentration at which the source and sink terms in Eq. (6) balance ($\frac{dNO_2^-}{dt} = 0$), and therefore also corresponds to the maximum NO_2^- concentration.

Simulated *CP* and *CPt* were compared to observed maximum NO_2^- concentrations and corresponding times. Equations (11) and (12) were used to calculate *AmOR* and *NiOR* at each time step, and an instantaneous coupling index (*ICI*) given by the *NiOR*:*AmOR* ratio at a given

time, where $ICI < 1$ indicates uncoupled conditions. A cumulative coupling index (*CCI*) was also calculated from the ratio of time-integrated *NiOR* and *AmOR*, which expresses the percentage of NO_2^- produced by *AmO* that was subsequently oxidized by *NiO*.

Robust parameter selection methods were implemented to constrain the number of parameters (described in detail in SI). For parameters that varied with temperature, functional relationships with temperature were determined by non-linear regression (SigmaPlot). Activation energies (E_a) obtained from Arrhenius plots are reported when the natural logarithms of parameter values were correlated with the reciprocal of absolute temperature at $P < 0.05$. Values of μ_{Amo} and μ_{NiO} were also fitted to the macromolecular rate theory (MMRT) model (Hobbs et al., 2013) (details in SI).

3. Results

3.1. Experiment

Temporal trends in N and pH dynamics, and temperature effects on these dynamics, were similar for soils A and B (Fig. 2). Soil NH_4^+ concentrations increased over time, increasing more slowly at colder temperatures, before reaching maxima and then starting to decline. During the period that soil NH_4^+ was increasing, volatilized NH_3 and soil pH increased, but more slowly at colder temperatures, followed by a period where NH_3 started to level off and soil pH decreased. Soil NO_3^- increased more slowly at colder temperatures before reaching maxima, except in soil B at ≤ 10 °C, where neither NH_3 nor NO_3^- appeared to level off by 84 d. The dynamics of NO_2^-, NO and N_2O were analyzed in greater detail. Soil NO_2^- increased before reaching its maximum concentration, or NO_2^- compensation point (*CP*), followed by a decline; the only exception was in soil B at 5 °C where no decline in NO_2^- was observed by 84 d. Under warmer conditions (≥15 °C), NO_2^- returned to baseline (<0.1 μg N g^{-1}), whereas at 5 and 10 °C soil NO_2^- remained elevated at 84 d. The *CP* and *CPt* were both affected by the interaction of temperature and soil type (Fig. 3a). The *CP* tended to be greater, and the *CPt* delayed, under colder conditions, and the *CPt* was well-described by exponential decay models (Fig. 3a). Averaged across temperatures, mean *CP* in soil A was nearly three times greater than in soil B.

All cumulative variables analyzed by ANOVA were affected by the interaction of temperature and soil type (Fig. 3b–c). Consistently in both soils, cumulative NO_2^- increased as temperature decreased from 30 to 10 °C, while cumulative NO_2^- at 5 °C was intermediate between the 10 and 15 °C values. Within each soil, cumulative NO exhibited similar temperature trends as cumulative NO_2^- and was positively correlated ($P <$

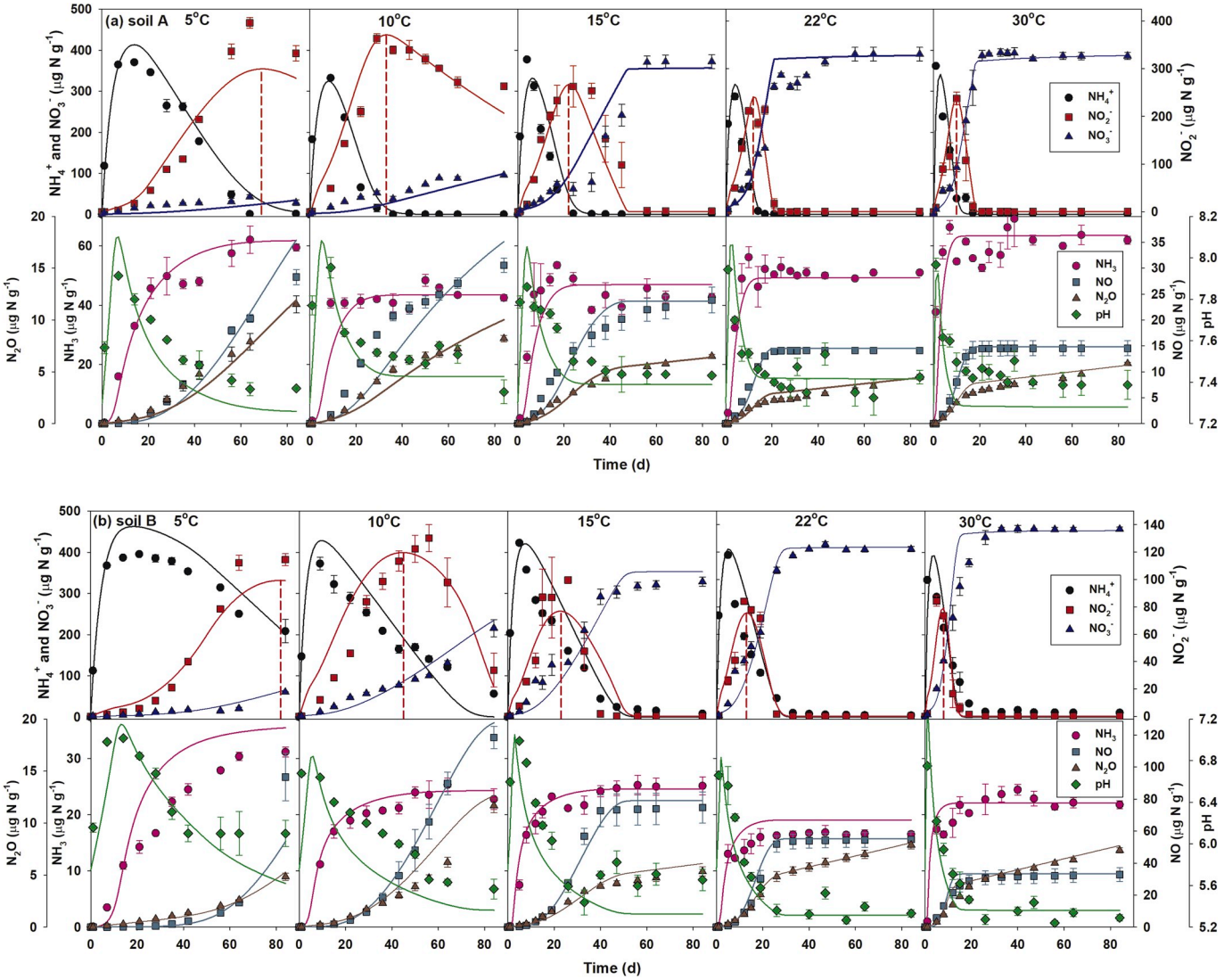

Fig. 2. Observed (symbols = means ± std error) and simulated (lines) nitrogen (N) species and pH in (a) soil A and (b) soil B at five temperatures. In the lower panes, 'NH_3' is cumulative N captured in the acid traps, and 'NO' and 'N_2O' are cumulative N determined by trapezoidal integration of production rates versus time. Vertical dashed lines in the upper panes indicate timing and magnitude of simulated nitrite compensation points (*CP*).

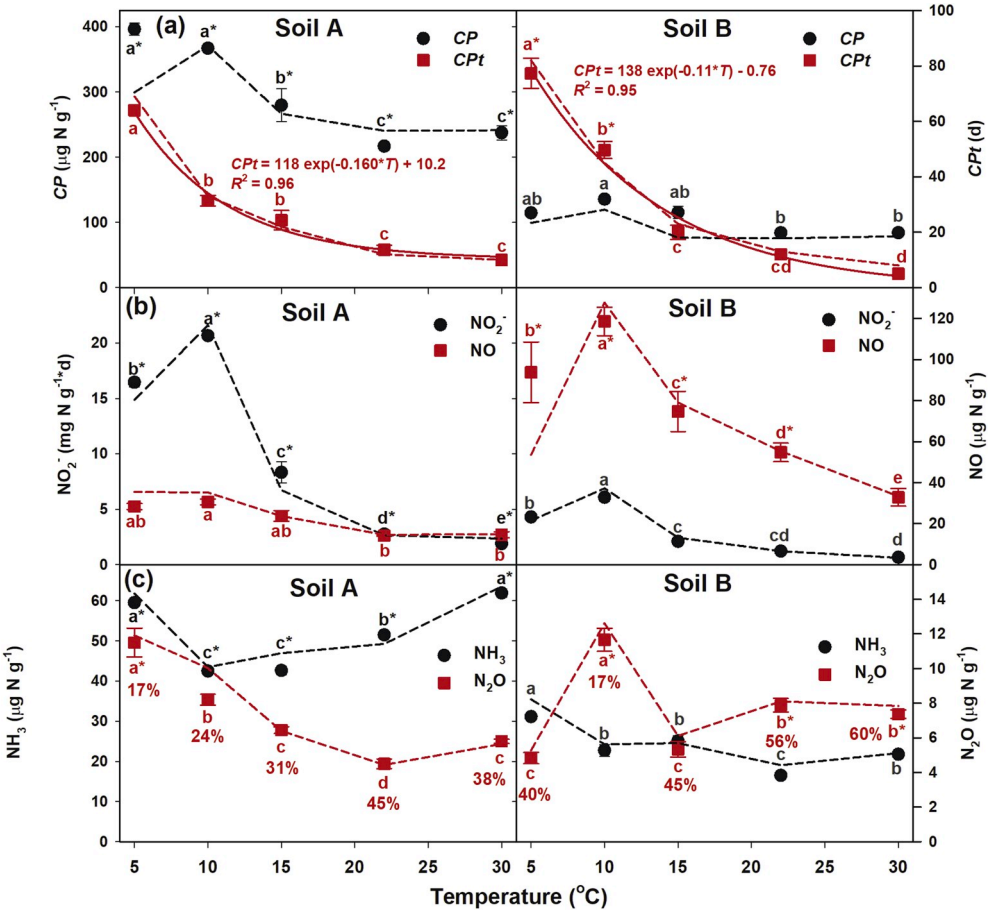

Fig. 3. Observed (symbols = means ± std error) and simulated (lines) (a) nitrite compensation point (*CP*) and time to reach *CP* (*CPt*), (b) cumulative NO_2^- and NO, and (c) cumulative NH_3 and N_2O in soils A and B. Within each soil, means with same letter do not differ by temperature at $P < 0.05$. An asterisk (*) indicates a mean is greater compared to other soil at the same temperature at $P < 0.05$. In (a), solid lines are exponential decay functions based on regression of observed *CPt* versus temperature. In (c), the values below each symbol are the percentages of the total simulated N_2O production due to zero-order production (b_{N_2O} in Eq. (9)).

0.001) with cumulative NO_2^- in soil A ($r^2 = 0.87$) and B ($r^2 = 0.80$). In contrast to cumulative NO_2^-, which was two to four times greater at a given temperature in soil A than B, cumulative NO was two to four times greater in soil B than A (Fig. 3b). Trends in cumulative N_2O were less consistent with the trends in cumulative NO_2^- compared with cumulative NO (Fig. 3c). Cumulative N_2O was positively correlated ($P < 0.001$) with cumulative NO_2^- in soil A ($r^2 = 0.58$), while less strongly in soil B ($r^2 = 0.20$, $P = 0.10$). When data from 5 °C were excluded, the degree of correlation between cumulative NO_2^- and N_2O increased ($r^2 = 0.79$ and 0.61 in soils A and B, respectively). Cumulative N_2O reached its maximum value at 5 °C in soil A and at 10 °C in soil B, which had greater cumulative N_2O at 10, 22 and 30 °C compared to soil A. Cumulative NH_3 was two to three times greater in soil A than B at each temperature, and there were differences in cumulative NH_3 by temperature, but the pattern of differences was not consistent across soil types (Fig. 3c).

Recovery of N inputs after 84 d ranged from 86 to 101% (Table 2). At and above 15 °C, NO_3^- was the dominant form of recovered N, while NO_2^- and/or NH_4^+ were recovered increasingly at ≤ 10 °C. Cumulative NO

Table 2
Recovery of nitrogen (N) after 84 days of incubation accounting for measured and simulated variables.

Temp	Input[b]	[a]Percent recovery of urea + mineralized N as:								
		Remaining in soil			Cumulative gases emitted			Total without NO_2^- sink	NO_2^- sink[c]	Total with NO_2^- sink
		NH_4^+	NO_2^-	NO_3^-	NH_3	NO	N_2O			
°C	µg Ng^{-1}						%			
Soil A										
5	507.5	11.7 (0.3)	65.5 (4.5)	5.6 (1.8)	11.7 (0.3)	5.6 (0.40)	2.3 (0.23)	91.0 (2.9)	15.8	106.9 (2.9)
10	509.5	8.3 (0.3)	51.7 (0.4)	18.7 (0.2)	8.3 (0.3)	6.0 (0.38)	1.6 (0.09)	86.4 (0.6)	22.9	109.4 (0.6)
15	512.0	8.3 (0.3)	<0.5	72.4 (4.2)	8.3 (0.3)	4.6 (0.72)	1.3 (0.05)	87.6 (3.2)	15.7	103.3 (3.2)
22	516.7	10.0 (0.2)	<0.5	75.5 (4.6)	10.0 (0.2)	2.7 (0.07)	0.87 (0.08)	89.6 (3.3)	12.3	101.9 (3.3)
30	524.4	11.8 (0.4)	<0.5	73.6 (2.4)	11.8 (0.4)	2.8 (0.39)	1.1 (0.03)	89.8 (1.9)	10.7	100.5 (1.9)
Soil B										
5	508.0	41.0 (7.9)	22.5 (1.2)	11.9 (0.3)	6.1 (0.3)	18.5 (4.1)	1.0 (0.09)	101.3 (5.9)	9.4	110.6 (5.9)
10	510.1	11.1 (1.2)	6.6 (3.4)	42.3 (5.8)	4.5 (0.5)	23.2 (1.9)	2.3 (0.18)	90.2 (6.6)	17.8	108.0 (6.6)
15	512.8	1.6 (0.2)	<0.5	64.0 (3.0)	4.9 (0.4)	14.6 (2.7)	1.0 (0.12)	86.4 (0.9)	10.2	96.6 (0.9)
22	517.8	0.8 (0.3)	<0.5	78.7 (1.7)	3.2 (0.1)	10.6 (1.2)	1.5 (0.11)	95.0 (0.8)	5.4	100.4 (0.8)
30	525.9	2.0 (0.4)	<0.5	86.7 (1.4)	4.1 (0.2)	6.2 (1.2)	1.4 (0.07)	100.8 (0.4)	2.8	103.6 (0.4)

[a] Values are means of three replicates (±standard error) except for single value of NO_2^- sink simulated for each soil and temperature combination.
[b] Includes 500 µg Ng^{-1} of added urea plus the simulated contribution from N mineralization over 84 days.
[c] Total cumulative amount over 84 d simulated by the $k_f NO_2$ term in Eq. (6) as a percentage of N input.

accounted for <6% of N inputs in soil A compared to 6–23% in soil B, while recovery as N_2O was similar in both soils. Cumulative NH_3 accounted for 8–12% in soil A compared to <6% in soil B.

3.2. Modeling

The model captured the overall trends in time series and cumulative data (Figs. 2 and 3). In particular, the trend of increasing *CPt* with decreasing temperature was accurately simulated (Fig. 3a) with mean-normalized root-mean square errors (RMSE) of 9 and 11% for soils A and B, respectively. Trends in mean *CP* with temperature were simulated with RMSEs of 15 and 19%, respectively; although the model underestimated *CP* at 5 °C in soil A and 22 °C in soil B by 24 and 33%, respectively (Fig. 3a). Cumulative NO_2^-, NO and N_2O were simulated with RMSEs of 11 and 15%, 17 and 25% and 11 and 9%, for soils A and B, respectively (Fig. 3b and c). The largest discrepancies between simulated and observed data occurred at 5 °C for cumulative N_2O in soil B (underestimated by 43%), at 5 °C for cumulative NO in soil A (overestimated by 25%) and at 30 °C for cumulative NO_2^- in soil A (overestimated by 24%). Cumulative NH_3 responses were simulated with RMSEs of 5 and 10% in soils A and B, respectively, with the largest discrepancies occurring at 5 and 22 °C in soil B where the model overestimated observed means by 14 and 15%, respectively. For soil A, NO and N_2O production were simulated more accurately when NO_2^- was used as the substrate in Eqs. (8) and (9), whereas using HNO_2 as the substrate resulted in better model performance for soil B.

Simulations done at 5 °C without the use of Eq. (13) resulted in substantial overestimation of NO_2^- concentrations during the first 60 d (Fig. 2S). Therefore, Eq. (13) was used in the final simulations at 5 °C to account for increases in ammonia-oxidizing microbial populations and/or enzyme activities over time. Simulations done without inclusion of the $k_f NO_2$ term in Eq. (6) resulted in good model agreement with the NO_2^-, NO and N_2O data, but there was significant over-estimation of NO_3^- in most cases (Fig. 2S). The additional NO_2^- sink ($k_f NO_2$) included

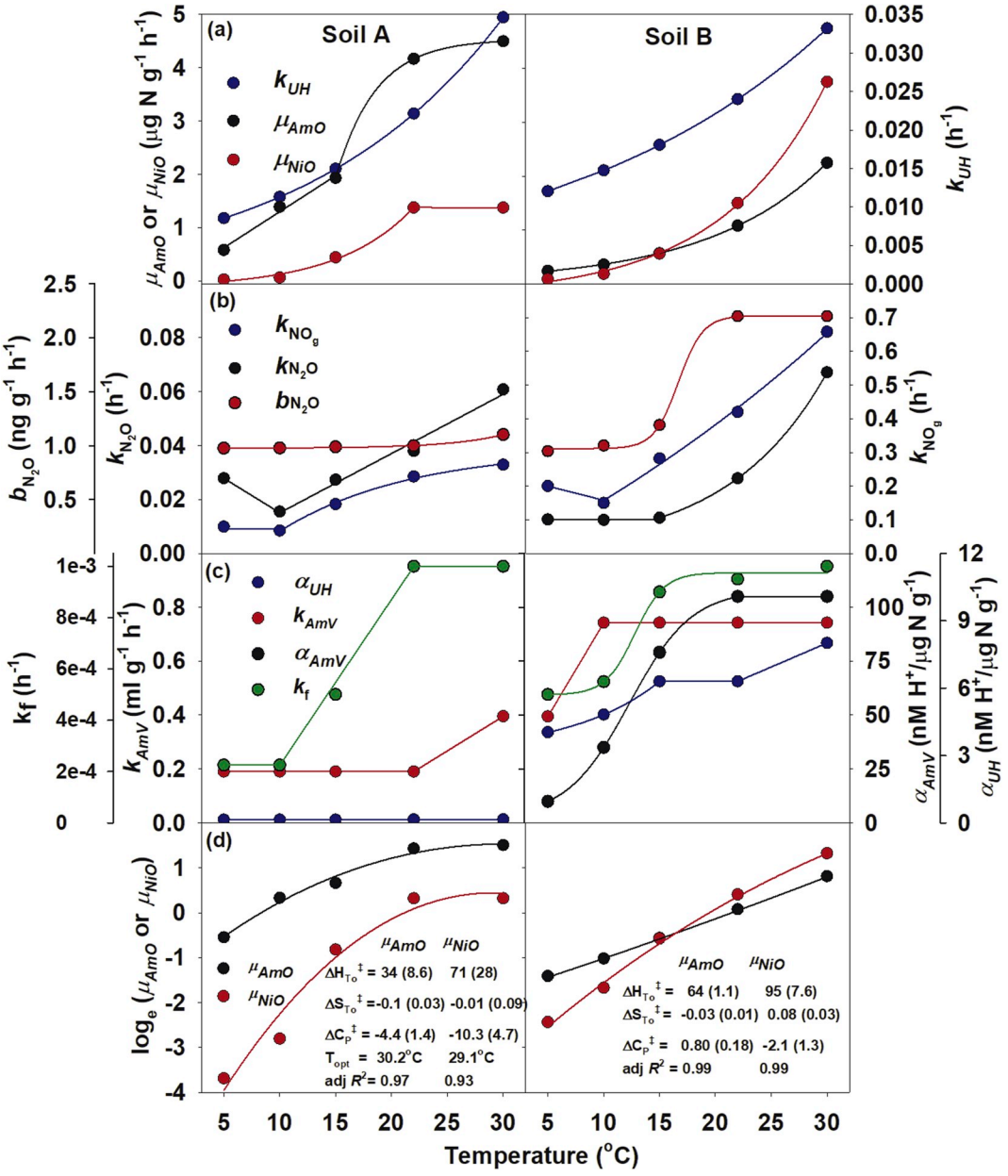

Fig. 4. Best-fit parameter values (symbols) and regression functions (lines) for parameters that vary by temperature for soil A (left) and soil B (right). Lines in panes (a) thru (c) are the temperature functions reported in Table 1. Lines in (d) are model fits with estimated regression coefficients for the MMRT model (Eq. 5S, see SI).

in the final model accounted for 3–23% of total N inputs and moved the estimates of total N recovery closer to 100% in 8 of 10 cases compared to estimates based on measured variables, in soil B at 5 and 30 °C (Table 2). In both soils, the cumulative sink was greatest at 10 °C and least at 30 °C, and was positively correlated with cumulative NO_2^- ($r^2 = 0.83$–0.84, $P \leq 0.03$).

In general, parameters that varied with temperature could be expressed as increasing functions of temperature (Table 1, Fig. 4). Some parameters were constant over specific ranges, and in two cases, values were greater at 5 than at 10 °C (k_{N_2O} in soil A and k_{NO_g} in soil B). Some parameters were best described using different functions over different temperature ranges. Activation energies (E_a) were obtained for all parameters that varied with temperature (Table 1), except α_{UH} in soil A and k_{AmV} in both soils, for which Arrhenius relationships were not significant. In some cases, significant relationships were found only when the temperature range was constrained to ≥10 °C or ≤22 °C. The E_a values for several parameters (k_{UH}, k_{NO}, k_{N_2O}, μ_{AmO} and μ_{NiO}) were similar (within ±11%) between soils, whereas E_a for k_f and b_{N_2O} differed more widely by soil. Arrhenius plots for μ_{AmO} and μ_{NiO} were significant across 5–30 °C in soil A ($r^2 = 0.88$ and 0.91, respectively) and B ($r^2 > 0.99$). In both soils, E_a for μ_{NiO} exceeded the E_a for μ_{AmO} by factors of 2.1 and 1.7 in soils A and B, respectively. Compared to Arrhenius plots, the MMRT model described temperature responses better in soil A based on R^2 (Fig. 4d). Optimum temperature (T_{opt}) values were obtained for soil A (Fig. 4d), but in soil B could not be obtained for μ_{AmO} and the obtained value for μ_{NiO} (68 °C) was not biologically feasible.

Model-simulated *NiOR* initially lagged behind *AmOR* but eventually equaled and then exceeded *AmOR* (Fig. 3S). The *ICI* was initially <100%, indicating uncoupling that persisted for longer periods at colder temperatures (Fig. 5a). Once the point of coupling (*ICI* = 100%) was reached, *ICI* then increased above 100% (note that *ICI* values > 100% are not shown in Fig. 5a to improve visibility of data prior to reaching 100%). The time required to reach coupled conditions decreased exponentially with temperature while *CCI* increased with temperature (Fig. 5b).

4. Discussion

The first and second steps of nitrification, *AmO* and *NiO*, were increasingly uncoupled at colder temperatures as evidenced by increased cumulative NO_2^- that was associated with increased production of NO, and to a lesser extent N_2O. Maximum NO_2^- concentrations tended to increase and elevated NO_2^- concentrations persisted for longer periods at decreasing temperature. These results imply that *NiOR* was more sensitive to temperature than *AmOR*. This hypothesis is supported by the model results. Differential temperature sensitivities are apparent in the relationships in Fig. 4d, where μ_{NiO} declined faster with decreasing temperature than μ_{AmO} in both soils and in the greater E_a estimates for μ_{NiO} compared to μ_{AmO} (Table 1). However, μ_{AmO} and μ_{NiO} do not necessarily represent the actual rates at any point in time, which also depend on substrate levels and the other parameters in Eq. (11) and (12). The model-calculated rates (Fig. 3S), and ratios between those rates expressed as *ICI* and *CCI* (Fig. 5), show that simulated *NiOR* decreased relative to *AmOR* at decreasing temperature, which also support the hypothesis that differential temperature responses of *AmOR* and *NiOR* were a fundamental regulator of the observed patterns.

The best-fit μ_{NiO} values obtained here at 30 °C (1.4–3.8 μg N g^{-1} h^{-1}) are similar to Michaelis-Menten (V_{max}) values obtained by Taylor et al. (2019), whereas our K_{NiO} values were ~10 times less than their estimates (1.7–2.2 μM after unit conversion). The latter difference may result from the fact that Taylor et al. (2019) used slurries compared to unsaturated soils used here. Taylor et al. (2019) concluded that differential temperature responses of V_{max} for *NiO* compared to *AmO*, previously measured by Taylor et al. (2017), were likely not responsible for NO_2^- accumulation in their experiments. They observed that *NiO* substrate affinities responded to temperature, although the directions of the

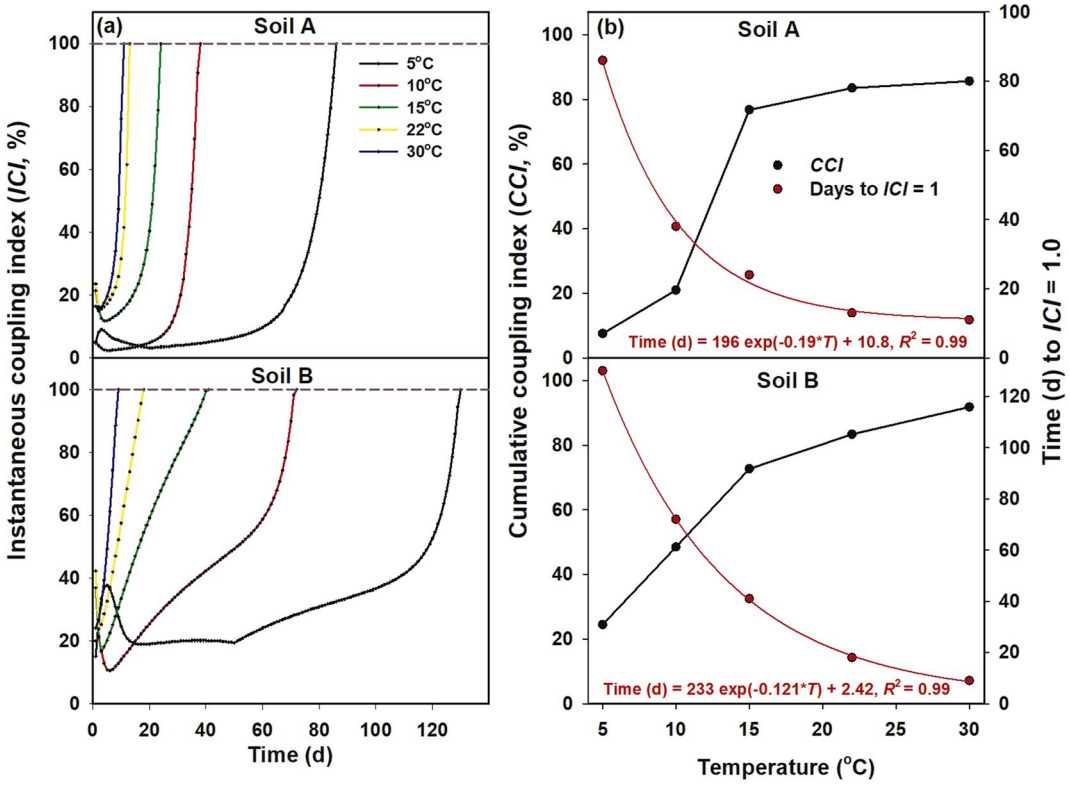

Fig. 5. Model-simulated (a) instantaneous coupling index (*ICI*) versus time and (b) cumulative coupling index (*CCI*) and time at which *ICI* reaches 100% with regression lines versus temperature. In (a), *ICI* values > 100%, which correspond to coupled conditions falling above dashed horizontal lines, are not shown to improve visibility of the data occurring prior to reaching 100%. In (b), *CCI* is plotted on the left axis, and time on the right axis.

responses were not consistent among soils. We found that using constant values for K_{NiO} across temperature were adequate to simulate NO_2^- dynamics. Our sensitivity analyses show that varying K_{NiO} over the range of 10%–200% of the values in Table 1 altered cumulative NO_2^- estimates by <2.5% in soil A and <12% in soil B.

Another relevant observation of Taylor et al. (2019) is that, under the assumption of Michaelis-Menten kinetics, NO_2^- must increase to some extent following NH_4^+ addition before *NiOR* can equal *AmOR* which further highlights that kinetic parameters alone do not determine process rates. In soil B at ≤ 15 °C, μ_{NiO} was ≥ μ_{AmO}, which might imply low potential for NO_2^- to accumulate; yet NO_2^- increased to >70 μg N g^{-1} and remained elevated for weeks. An advantage of dynamic simulations is that they can account for effects of varying substrate levels on process rates that cannot be determined based on knowledge of kinetic parameters alone.

Venterea and Rolston (2000b) simulated both steps of nitrification using kinetics that accounted for Monod-based population growth. Here, population growth models were not required to simulate the characteristic 'rise and fall' pattern of NO_2^- dynamics, except at 5 °C, possibly indicating that growth of cold-adapted populations of ammonia oxidizers was important. The usefulness of the uncompetitive NH_3 inhibition model (Eqs. (11) and (12)) used here does not preclude the potential importance of other inhibitory or competing agents (Boon and Laudelout, 1962; Hunik et al., 1993). In our preliminary simulations (SI), we evaluated inhibition of *AmO* by low pH and of *NiO* by high pH (Hawkins et al., 2010), but predictions of these models did not correspond with observations. The uncompetitive inhibition model used here was also found by Park and Bae (2009) to best describe nitrification kinetics affected by NH_3 inhibition in wastewater. However, the current experiments were not primarily designed to distinguish among different types of inhibition kinetics which could be addressed more directly using techniques similar to those used by Park and Bae (2009). Also, the inhibition models applied here are likely a simplification of kinetics resulting from activities of different sub-populations of ammonia-oxidizing bacteria and/or archaea, and nitrite-oxidizing bacteria, each of which may have differing maximum utilization potentials, substrate affinities, sensitivities to inhibitory agents and/or responses to temperature (Giguere et al., 2017; Duan et al., 2018; Lu et al., 2018; Taylor et al., 2019). Thus, values of the model parameters in Eqs. (11) and (12), and their variation with temperature, represent 'average' behavior across populations. Some studies indicate that *AmO* carried out by archaea, and complete nitrification ('comammox') carried out by some strains of *Nitrospira*, are more important under conditions of low N availability, and therefore may not have been important in the current experiment (Di et al., 2009; Wang et al., 2019). Nonetheless, it is likely that substantial diversity in kinetic behavior exists within strains of soil bacteria which separately carry out *AmO* and *NiO*. Similarly, while NO and N_2O production are each simulated here using single rate coefficients, they can be generated via multiple processes, both biologically and abiotically, with NO_2^- and/or HNO_2 as proposed substrates (Wrage et al., 2001; Wei et al., 2017). Nitric oxide has recently been identified NO as an obligate intermediate of hydroxylamine (NH_2OH) oxidation by autotrophic ammonia oxidizing bacteria (Caranto and Lancaster, 2017). Caranto and Lancaster (2017) also proposed that, under oxygen stress, production of intracellular NO may exceed its rate of oxidation to NO_2^- and that this could result in atmospheric emissions of NO and/or its conversion to N_2O. The current modeling scheme does not explicitly account for these potential pathways, which may or may not have been important under the aerobic incubation conditions. The mechanisms considered here assume (i) that NO_2^- accumulates due to the inability of *NiOR* to fully process NO_2^- produced via *AmOR*, and (ii) that NO production occurs mainly via biological and/or abiotic reduction of NO_2^- based on the rapid production of NO (and N_2O) observed in both sterile and non-sterile soils under aerobic conditions following addition of NO_2^- (Venterea and Rolston, 2000a; Wei et al., 2017). Incorporating the pathway of NO (and N_2O) emissions proposed by Caranto and Lancaster (2017) into the *2SN* model might allow for hypothesis testing, for example, by comparing simulations to observation made under varying O_2 availability. This would likely require explicit incorporation of the individual steps in *AmO*, including $NH_2OH \rightarrow NO \rightarrow NO_2^-$, into the model, as well as additional measurements (e.g., NH_2OH). For biological N_2O production, the relative contributions of ammonia-oxidizing bacteria and archaea, and their respective kinetics, may vary with chemical conditions and nitrite-oxidizing activity (Giguere et al., 2017) and/or temperature (Xu et al., 2017). While the use of single kinetic expressions to simulate *AmO*, *NiO*, and NO and N_2O production was an efficient approach for the current application, additional modeling studies could determine if explicitly accounting for process-level diversity would provide additional insight.

While the two soils exhibited similar dynamics and temperature responses, there were notable differences in the magnitude of those responses. Soil A had consistently greater cumulative NO_2^- and NH_3 volatilization than soil B, both of which were likely driven by a greater pH in soil A, which shifts the NH_4^+-NH_3 equilibrium toward NH_3. Conversely, despite greater cumulative NO_2^-, soil A had substantially less cumulative NO production at all temperatures except 30 °C, and less cumulative N_2O at 10, 22 and 30 °C. This effect could have been driven by the lower pH in soil B, which shifts the NO_2^--HNO_2 equilibrium toward HNO_2, which is known to favor abiotic NO production and at least hypothesized to favor abiotic N_2O production (Thorn and Mikita, 2000). Obtained values of model parameters for the two soils were of similar magnitude, particularly for k_{UH}, K_{NiO}, μ_{NiO} at ≤ 22 °C and k_f at ≥ 22 °C (Table 1, Fig. 4). In contrast, the pH-regulating parameters (α_{UH}, α_{AmV} and α_{AmO}) were consistently 10 to 100 times less in soil A than B reflecting the greater apparent pH buffering capacity of soil A. Alternative methods for simulating pH consider buffering capacity explicitly (Wang et al., 1998). Such pH simulation methods that utilize independent estimates of pH buffering capacity might improve the robustness of the pH component of the *2SN* model and reduce the number of parameters requiring estimation.

Inclusion of the sink term $k_f NO_2$ in Eq. (6) is a hypothesis to account for the overestimation of NO_3^- accumulation that was simulated without this term (Fig. 2S) and for the incomplete recovery of N in measured forms (Table 2). Further work is needed to test this or alternative hypotheses. A possible pathway for the unmeasured loss is abiotic incorporation or 'fixation' of NO_2^- into phenolic and/or humic fractions of soil organic matter. Fitzhugh et al. (2003) found that 30–60% of ^{15}N-labelled NO_2^- applied to three O-horizon forest soils was fixed within 15 min of application and 25–50% was retained after 28 d. The amounts fixed by the mineral soils studied here were likely substantially less than that. However, the same processes involved in NO_2^- incorporation into soil organic matter, including nitrosation, can also produce N gases including N_2O, dinitrogen (N_2) and methyl nitrite (CH_3ONO) (Stevenson and Swaby, 1964; Thorn and Mikita, 2000; Wei et al., 2017). Thus, the potential for these processes to contribute to unmeasured N loss pathways is greater than the potential amount of fixed NO_2^-. In addition, the protonated form of NO_2^- (HNO_2 or HONO) can also be emitted as a gas (Su et al., 2011). An alternative hypothesis is an unmeasured sink for NO_3^-, such as immobilization of NO_3^- (Fitzhugh et al., 2003) or heterotrophic denitrification. This possibility was examined in separate simulations that included a sink term for NO_3^- in Eq. (7), which did not improve model performance. Wertz et al. (2018) found evidence for denitrification in frozen soil (≤0.5 °C), amended with inorganic N and plant residues (1000 μg C g^{-1}), and incubated at a headspace:soil ratio of 4.2 ml g^{-1} dry soil (compared to 25 ml g^{-1} used here). Under these conditions, increasing NO_2^- over time was accompanied by decreasing NO_3^-, which was not observed here, and was likely driven by O_2 depletion in occluded microsites (Wertz et al., 2018). The apparent background N_2O production (b_{N_2O}, Eq. (9)) was simulated here as being independent of NO_2^- and may have originated from microsite denitrification. However, given the highly aerobic conditions, this source more likely evolved from NO_2^- present at levels that were below detection

and/or from other nitrification-driven reactions such as those involving NH_2OH (Liu et al., 2017a). Cumulative amounts of background N_2O ranged from 2 to 4 μg N g^{-1} and therefore could not explain the unaccounted-for NO_3^- (Fig. 2S) although it did account for 17–60% of total simulated cumulative N_2O (Fig. 3c).

The MMRT model was useful for expressing μ_{NiO} and μ_{AmO} as continuous functions of temperature, which was the main objective. Of secondary interest was estimation of optimum temperatures which were only obtained for soil A. The optimum temperature estimates are likely not robust due to the limited upper temperature range, which was also the likely reason for the lack of curvature in the MMRT results for soil B. Nonetheless, the MMRT functions and the functions obtained for the other parameters, allow the model, in theory, to be applied under dynamic temperature regimes at least for temperatures $\leq$30 °C (an example application is provided as SI and the results are shown in Fig. 4S). While *2SN* can account for multiple process interactions, in its current form it is restricted to well-mixed, primarily aerobic soil volumes. While this application is useful for testing hypotheses and exploring mechanisms and kinetics, to extend its applicability, *2SN* would need to be integrated with models that account for other processes occurring over a broader range of conditions. These processes, which are addressed by other models, include diffusion of solutes and gases (Venterea and Rolston, 2000b), water flux, soil anaerobicity and heterotrophic denitrification (Riley and Matson, 2000) and plant N uptake (Inselsbacher et al., 2013). Apart from the modeling aspects of the study, the empirical findings suggest that the presence of available N at cold temperatures may give rise to large N gas losses due to reactions involving NO_2^-. This further suggests that elevated N_2O emissions observed under colder temperatures in the field (Wagner-Riddle et al., 2008) might be at least partly driven by these processes, but this requires further investigation.

Declaration of competing interest

The authors declare that they have no known competing financial interests or personal relationships that could have appeared to influence the work reported in this paper.

Acknowledgements

The authors acknowledge and thank Dr. Emerson F.C. Souza, Michael Dolan, Xinci Tan and Carrie O'Connor-Walker for their assistance with the experiments, Scott Mitchell for logistical help and Dr. Larry Hendrickson and two anonymous reviewers for their review of an earlier draft of the manuscript. This work was supported in part by a grant from the Minnesota Corn Growers/Minnesota Corn Research and Promotion Council, and by the Agricultural Research Service under the Soil and Air National Program no. 212.

Appendix A. Supplementary data

Supplementary data to this article can be found online at https://doi.org/10.1016/j.soilbio.2020.107727.

References

Aleem, M.I., Alexander, M., 1958. Cell-free nitrification by nitrobacter. Journal of Bacteriology 76, 510–514.
Anthonisen, A.C., Loehr, R.C., Prakasam, T.B.S., Srinath, E.G., 1976. Inhibition of nitrification by ammonia and nitrous-acid. Journal Water Pollution Control Federation 48, 835–852.
Bates, R., Pinching, G., 1949. Acidic dissociation constant of ammonium ion at 0° to 50°C, and the base strength of ammonia. Journal of Research of the National Bureau of Standards 42, 419–430. Research Paper RP1982.
Boon, B., Laudelout, H., 1962. Kinetics of nitrite oxidation by Nitrobacter winogradskyi. Biochemical Journal 85, 440–447.
Breuillin-Sessoms, F., Venterea, R.T., Sadowsky, M.J., Coulter, J.A., Clough, T.J., Wang, P., 2017. Nitrification gene ratio and free ammonia explain nitrite and nitrous oxide production in urea-amended soils. Soil Biology and Biochemistry 111, 143–153.
Burns, L.C., Stevens, R.J., Smith, R.V., Cooper, J.E., 1995. The occurrence and possible sources of nitrite in a grazed, fertilized, grassland soil. Soil Biology and Biochemistry 27, 47–59.
Caranto, J.D., Lancaster, K.M., 2017. Nitric oxide is an obligate bacterial nitrification intermediate produced by hydroxylamine oxidoreductase. Proceedings of the National Academy of Sciences 114, 8217.
Carrera, J., Jubany, I., Carvallo, L., Chamy, R., Lafuente, J., 2004. Kinetic models for nitrification inhibition by ammonium and nitrite in a suspended and an immobilised biomass systems. Process Biochemistry 39, 1159–1165.
Chalk, P.M., Keeney, D.R., Walsh, L.M., 1975. Crop recovery and nitrification of fall and spring applied anhydrous Ammonia1. Agronomy Journal 67, 33–37.
Chapman, H.D., Liebig, G.F., 1952. Field and laboratory studies of nitrite accumulation in Soils1, 2. Soil Science Society of America Journal 16, 276–282.
Clough, T., Sherlock, R., Mautner, M.B., Milligan, D.F., Wilson, P., Freeman, C., McEwan, M., 2003. Emission of nitrogen oxides and ammonia from varying rates of applied synthetic urine and correlations with soil chemistry. Australian Journal of Soil Research 41.
Conrad, R., 1994. Compensation concentration as critical variable for regulating the flux of trace gases between soil and atmosphere. Biogeochemistry 27, 155–170.
Di, H.J., Cameron, K.C., Shen, J.P., Winefield, C.S., O'Callaghan, M., Bowatte, S., He, J. Z., 2009. Nitrification driven by bacteria and not archaea in nitrogen-rich grassland soils. Nature Geoscience 2, 621–624.
Duan, P., Wu, Z., Zhang, Q., Fan, C., Xiong, Z., 2018. Thermodynamic responses of ammonia-oxidizing archaea and bacteria explain N2O production from greenhouse vegetable soils. Soil Biology and Biochemistry 120, 37–47.
FAO, 2019. Food and Agriculture Organization of the United Nations. FAOSTAT: Fertilizers by Product ([WWW Document]).
Farquhar, G.D., Firth, P.M., Wetselaar, R., Weir, B., 1980. On the gaseous exchange of ammonia between leaves and the environment: determination of the ammonia compensation point. Plant Physiology 66, 710–714.
Fitzhugh, R.D., Lovett, G.M., Venterea, R.T., 2003. Biotic and abiotic immobilization of ammonium, nitrite, and nitrate in soils developed under different tree species in the Catskill Mountains, New York, USA. Global Change Biology 9, 1591–1601.
Giguere, A.T., Taylor, A.E., Suwa, Y., Myrold, D.D., Bottomley, P.J., 2017. Uncoupling of ammonia oxidation from nitrite oxidation: impact upon nitrous oxide production in non-cropped Oregon soils. Soil Biology and Biochemistry 104, 30–38.
Hawkins, S., Robinson, K., Layton, A., Sayler, G., 2010. Limited impact of free ammonia on Nitrobacter spp. inhibition assessed by chemical and molecular techniques. Bioresource Technology 101, 4513–4519.
Hobbs, J.K., Jiao, W., Easter, A.D., Parker, E.J., Schipper, L.A., Arcus, V.L., 2013. Change in heat capacity for enzyme catalysis determines temperature dependence of enzyme catalyzed rates. ACS Chemical Biology 8, 2388–2393.
Hunik, J., Meijer, H., Tramper, J., 1993. Kinetics of Nitrobacter agilis at extreme substrate, product and salt concentrations. Applied Microbiology and Biotechnology 40, 442–448.
Inselsbacher, E., Wanek, W., Strauss, J., Zechmeister-Boltenstern, S., Müller, C., 2013. A novel 15N tracer model reveals: plant nitrate uptake governs nitrogen transformation rates in agricultural soils. Soil Biology and Biochemistry 57, 301–310.
Kutner, M.H., Nachtsheim, C.J., Neter, J., 2004. Applied Linear Regression Models, 4 ed. McGraw-Hill, New York.
Liu, S.R., Berns, A.E., Vereecken, H., Wu, D., Bruggemann, N., 2017a. Interactive effects of MnO2, organic matter and pH on abiotic formation of N2O from hydroxylamine in artificial soil mixtures. Scientific Reports 7, 10.
Liu, Y., Wang, C., He, N., Wen, X., Gao, Y., Li, S., Niu, S., Butterbach-Bahl, K., Luo, Y., Yu, G., 2017b. A global synthesis of the rate and temperature sensitivity of soil nitrogen mineralization: latitudinal patterns and mechanisms. Global Change Biology 23, 455–464.
Lu, X., Nicol, G.W., Neufeld, J.D., 2018. Differential responses of soil ammonia-oxidizing archaea and bacteria to temperature and depth under two different land uses. Soil Biology and Biochemistry 120, 272–282.
Ma, L., Shan, J., Yan, X.Y., 2015. Nitrite behavior accounts for the nitrous oxide peaks following fertilization in a fluvo-aquic soil. Biology and Fertility of Soils 51, 563–572.
Maharjan, B., Venterea, R.T., 2013. Nitrite intensity explains N management effects on N_2O emissions in maize. Soil Biology and Biochemistry 66, 229–238.
Moyo, C.C., Kissel, D.E., Cabrera, M.L., 1989. Temperature effects on soil urease activity. Soil Biology and Biochemistry 21, 935–938.
Mulvaney, R.L., 1996. Nitrogen-inorganic forms. In: Sparks, D.L. (Ed.), Methods of Soil Analysis. Am. Soc. Agron., Madison, WI, pp. 1123–1184.
Park, S., Bae, W., 2009. Modeling kinetics of ammonium oxidation and nitrite oxidation under simultaneous inhibition by free ammonia and free nitrous acid. Process Biochemistry 44, 631–640.
Press, W.H., Teukolsky, S.A., Vetterling, W.T., Flannery, B.P., 2010. Numerical Recipes: the Art of Scientific Computing Is Written by William H. Press, Saul A. Teukolsky, William T. Vetterling, and Brian P. Flannery. Cambridge University Press. © 2007, hardback, ISBN 978-0-521-88068-8, 1235 pp. ACM SIGSOFT Software Engineering Notes 35, 30-31.
Riley, W.J., Matson, P.A., 2000. Nloss: a mechanistic model of denitrified N2o and N2 evolution from soil. Soil Science 165, 237–249.
Sánchez-Rodríguez, A.R., Nie, C., Hill, P.W., Chadwick, D.R., Jones, D.L., 2019. Extreme flood events at higher temperatures exacerbate the loss of soil functionality and trace gas emissions in grassland. Soil Biology and Biochemistry 130, 227–236.

Sherlock, R., Goh, K., 1985. Dynamics of ammonia volatilization from simulated urine patches and aqueous urea applied to pasture. II. Theoretical derivation of a simplified model. Fertilizer Research 6, 3–22.
Stevens, R.J., Laughlin, R.J., 1995. Nitrite transformations during soil extraction with potassium-chloride. Soil Science Society of America Journal 59, 933–938.
Stevenson, F., Swaby, R., 1964. Nitrosation of soil organic matter: I. Nature of gases evolved during nitrous acid treatment of lignins and humic substances 1. Soil Science Society of America Journal 28, 773–778.
Stojanovic, B.J., Alexander, M., 1958. Effect of inorganic nitrogen on nitrification. Soil Science 86, 208–215.
Su, H., Cheng, Y., Oswald, R., Behrendt, T., Trebs, I., Meixner, F.X., Andreae, M.O., Cheng, P., Zhang, Y., Pöschl, U., 2011. Soil nitrite as a source of atmospheric HONO and OH radicals. Science 333, 1616–1618.
Taylor, A.E., Giguere, A.T., Zoebelein, C.M., Myrold, D.D., Bottomley, P.J., 2017. Modeling of soil nitrification responses to temperature reveals thermodynamic differences between ammonia-oxidizing activity of archaea and bacteria. The ISME Journal 11, 896.
Taylor, A.E., Myrold, D.D., Bottomley, P.J., 2019. Temperature affects the kinetics of nitrite oxidation and nitrification coupling in four agricultural soils. Soil Biology and Biochemistry 136, 107523. https://doi.org/10.1016/j.soilbio.2019.107523.
Tenuta, Beauchamp, E., 2003. Nitrous oxide production from granular nitrogen fertilizers applied to a silt loam soil. Canadian Journal of Soil Science 83, 521–532.
Thorn, K.A., Mikita, M.A., 2000. Nitrite fixation by humic substances: nitrogen-15 nuclear magnetic resonance evidence for potential intermediates in chemodenitrification. Soil Science Society of America Journal 64, 568–582.
Venterea, R.T., 2007. Nitrite-driven nitrous oxide production under aerobic soil conditions: kinetics and biochemical controls. Global Change Biology 13, 1798–1809.
Venterea, R.T., Clough, T.J., Coulter, J.A., Breuillin-Sessoms, F., Wang, P., Sadowsky, M. J., 2015. Ammonium sorption and ammonia inhibition of nitrite-oxidizing bacteria explain contrasting soil N_2O production. Scientific Reports 5, 12153.
Venterea, R.T., Rolston, D.E., 2000a. Mechanisms and kinetics of nitric and nitrous oxide production during nitrification in agricultural soil. Global Change Biology 6, 303–316.
Venterea, R.T., Rolston, D.E., 2000b. Mechanistic modeling of nitrite accumulation and nitrogen oxide gas emissions during nitrification. Journal of Environmental Quality 29, 1741–1751.
Venterea, R.T., Rolston, D.E., 2000c. Nitric and nitrous oxide emissions following fertilizer application to agricultural soil: biotic and abiotic mechanisms and kinetics. Journal of Geophysical Research-Atmospheres 105, 15117–15129.
Venterea, R.T., Rolston, D.E.E., Cardon, Z.G., 2005. Effects of soil moisture, physical, and chemical characteristics on abiotic nitric oxide production. Nutrient Cycling in Agroecosystems 72, 27–40.
Wagner-Riddle, C., Hu, Q., Van Bochove, E., Jayasundara, S., 2008. Linking nitrous oxide flux during spring thaw to nitrate denitrification in the soil profile. Soil Science Society of America Journal 72, 908–916.
Wang, F., Bear, J., Shaviv, A., 1998. Modelling simultaneous release, diffusion and nitrification of ammonium in the soil surrounding a granule or nest containing ammonium fertilizer. European Journal of Soil Science 49, 351–364.
Wang, Z., Cao, Y., Zhu-Barker, X., Nicol, G.W., Wright, A.L., Jia, Z., Jiang, X., 2019. Comammox Nitrospira clade B contributes to nitrification in soil. Soil Biology and Biochemistry 135, 392–395.
Wei, J., Amelung, W., Lehndorff, E., Schloter, M., Vereecken, H., Brüggemann, N., 2017. N2O and NOx emissions by reactions of nitrite with soil organic matter of a Norway spruce forest. Biogeochemistry 132, 325–342.
Wells, N.S., Baisden, W.T., Clough, T.J., 2015. Ammonia volatilisation is not the dominant factor in determining the soil nitrate isotopic composition of pasture systems. Agriculture, Ecosystems & Environment 199, 290–300.
Wertz, S., Goyer, C., Burton, D.L., Zebarth, B.J., Chantigny, M.H., 2018. Processes contributing to nitrite accumulation and concomitant N2O emissions in frozen soils. Soil Biology and Biochemistry 126, 31–39.
Wrage, N., Velthof, G.L., van Beusichem, M.L., Oenema, O., 2001. Role of nitrifier denitrification in the production of nitrous oxide. Soil Biology and Biochemistry 33, 1723–1732.
Xu, X., Liu, X., Li, Y., Ran, Y., Liu, Y., Zhang, Q., Li, Z., He, Y., Xu, J., Di, H., 2017. High temperatures inhibited the growth of soil bacteria and archaea but not that of fungi and altered nitrous oxide production mechanisms from different nitrogen sources in an acidic soil. Soil Biology and Biochemistry 107, 168–179.